Available online at www.sciencedirect.com
SCIENCE DIRECT®
Journal of Solid State Chemistry 177 (2004) 1965–1975
JOURNAL OF SOLID STATE CHEMISTRY
http://elsevier.com/locate/jssc

Crystal structure refinements of the three-layer Aurivillius ceramics $Bi_2Sr_{2-x}A_xNb_2TiO_{12}$ ($A = Ca, Ba$, $x = 0, 0.5, 1$) using combined X-ray and neutron powder diffraction

M.S. Haluska and S.T. Misture*

New York State College of Ceramics at Alfred University, 2 Pine St., Alfred, NY 14802-1296, USA

Received 29 August 2003; received in revised form 11 January 2004; accepted 16 January 2004

Abstract

Three-layer Aurivillius ceramics $Bi_2SrCaNb_2TiO_{12}$, $Bi_2Sr_{1.5}Ca_{0.5}Nb_2TiO_{12}$, $Bi_2Sr_2Nb_2TiO_{12}$, $Bi_2Sr_{1.5}Ba_{0.5}Nb_2TiO_{12}$, and $Bi_2SrBaNb_2TiO_{12}$ were formed via solid-state synthesis and their structures characterized by combined Rietveld analysis of powder X-ray and neutron diffraction data. Static disorder was observed in the form of mixed cation occupancies between the Bi and the Sr, Ca, or Ba on the *A* sites in the perovskite block, as well as between the Nb and Ti sites. The degree of site mixing between the Bi site in the $(Bi_2O_2)^{2+}$ layer and the perovskite-block *A* site increased with increasing average *A* site cation radius (ACR). $Bi_2SrBaNb_2TiO_{12}$ displayed the greatest degree of Bi–A site static disorder. Bond valence sum (BVS) calculations showed an increase in *A* site BVS with average *A* site cation radius. All compositions except $Bi_2SrCaNb_2TiO_{12}$ had overbonded *A* sites and the *A* site BVS increased nearly linearly with lattice parameter and ACR. A preference was observed for Ca^{2+} to remain on the *A* site while Ba^{2+} preferred to disorder to the Bi site, indicating that the cation site mixing occurs to reduce strain between the $(Bi_2O_2)^{2+}$ layer and the perovskite block in the structure. Unusually large Ti site BVS and thermal parameter for the equatorial oxygen in the TiO_6 octahedra were observed in structural models that included full oxygen occupancy. However, excellent structure models and more reasonable BVS values were obtained by assuming oxygen vacancies in the TiO_6 octahedra. AC impedance spectroscopy performed on all samples indicate that the total electrical conductivity is on the order of 10^{-4} S/cm at 900°C.
© 2004 Elsevier Inc. All rights reserved.

Keywords: Aurivillius; Site mixing; Static disorder

1. Introduction

The Aurivillius crystal structure was discovered by Aurivillius in 1949 [1]. It takes the form $Bi_2A_{n-1}B_nO_{3n+3}$ where the structure consists of $n-1$ perovskite layers that are stacked between bismuth oxide $(Bi_2O_2)^{2+}$ sheets. The Bi^{3+} cations in the $(Bi_2O_2)^{2+}$ layer have a lone pair of electrons which extend towards the perovskite *A* site cation and exert stereochemical repulsion from the surrounding oxygen anions. The cubo-octahedral Aurivillius *A* site can be occupied by Bi^{3+} [1], Sr^{2+}, Ba^{2+}, Ca^{2+} [2], La^{3+}, Pb^{2+} [3], K^+ [4], etc. The octahedral *B* site is much more size restrictive and is typically occupied by Ti^{4+} [1], Nb^{5+} [2], Ta^{5+} [5], W^{6+} [6], Ga^{3+} [7], Al^{3+} [7], or Mn^{3+} [8]. Aurivillius phases have been reported in the one-, two-, three-, and four-layer variants [2,9–11].

Aurivillius ceramics are interesting ferroelectrics [12,13] and have been studied for possible technological applications as oxygen ion conductors [4,7,14–18]. A number of crystal structure models have been published [2,5,9,10,19–21]. An interesting feature of the Aurivillius structure is that some compositions allow cation site mixing among atom positions, most notably between the Bi and perovskite *A* site [2,5,9,10]. Site mixing is not uncommon in layered structures and has been observed in alloys, pyrochlores [22,23], double-perovskites [24,25], and spinel type structures [26]. Site mixing in the Aurivillius structure was first observed by Blake et al. [2] for the two-layer ($n = 2$) phases and later confirmed by Hervoches et al. [9] in the three-layer ($n = 3$) phases. Early studies suggested that Bi^{3+} could only be replaced in small degree by another lone-pair cation such as Pb^{2+} [3]. However, it was later determined that other cations

*Corresponding author. Fax: +1-2-607-871-2354.
E-mail addresses: msh1@alfred.edu (M.S. Haluska), misture@alfred.edu (S.T. Misture).

0022-4596/$ - see front matter © 2004 Elsevier Inc. All rights reserved.
doi:10.1016/j.jssc.2004.01.010

lacking the lone pair such as the alkaline earths Sr^{2+}, Ba^{2+}, and Ca^{2+}, could occupy the Bi site [2].

Blake and Lightfoot [2] used Rietveld refinements of neutron data to show that in the two-layer Aurivillius structure $BaBi_2Nb_2O_9$, the Bi and *A* sites were of mixed occupancy. Furthermore, they observed that the degree of static disorder increased as the size of the substituted *A* site cation increased from Ca^{2+} to Sr^{2+} to Ba^{2+}. Macquart et al. [5] performed analogous work to Blake et al. in the $ABi_2Ta_2O_9$ system with similar results. Since the work of Blake et al. [2] site mixing has been observed in the two-, three-, and four-layer Aurivillius systems [9–11].

It is well known that the stability of perovskite related structures is governed in large part by geometric considerations and tolerance factors such as those developed by Goldschmidt [27] are useful in understanding structural stability. Tolerance factors were first used by Subbarao [12] with limited success to describe Aurivillius ceramics. Suarez et al. [28] were able to correlate tolerance factor with the paraelectric to ferroelectric phase transition but did not discuss structural stability. A special set of tolerance factors specific to the Aurivillius structure were developed by Speakman [17] which could predict with reasonable accuracy the structural stability in three-layer Aurivillius ceramics. Armstrong and Newnham [29] were the first to realize that the stable Aurivillius structure can sustain lattice strains between the $(Bi_2O_2)^{2+}$ sheets and the perovskite blocks. Furthermore, they developed an empirical equation using the perovskite block cation sizes to describe an ideal *a* lattice parameter.

Blake et al. [2] gave evidence in the form of bond valence sum (BVS) calculations to explain the static disorder in the $n = 2$ layer phases. They stated that the driving force behind the disorder was the overbonding of the Aurivillius *A* site and noted that replacement of the alkaline earth on the *A* site by the smaller Bi^{3+} cation reduces the overbonding.

Analysis of the BVS studies pertaining to Aurivillius ceramics reveals two types of structures; those with underbonded *A* sites [6,19,30–32]. and those with overbonded *A* sites [2,5,9,10,33]. The structures with underbonded *A* sites are the prototype Aurivillius structures such as $Bi_4Ti_3O_{12}$, Bi_3TiNbO_9, and Bi_2WO_6 where alkaline earths have not been substituted for Bi^{3+}. The prototype structures are orthorhombic or monoclinic and relieve the *A*-site underbonding by octahedral tilting or rotation, but not by site mixing [6]. Lightfoot et al. [31] analyzed $Bi_4Ti_3O_{12}$ via high-temperature neutron powder diffraction and found that the *A* site BVS decreased from a neutral valence of 3 in the orthorhombic symmetry low-temperature form to a strongly underbonded 2.22 state in the high-temperature tetragonal symmetry.

The structures with overbonded *A* sites include those where an alkaline earth replaces Bi^{3+} on the *A* site. $SrBi_2Nb_2O_9$ and $Bi_2Sr_2Nb_2TiO_{12}$ are two examples. Structures with overbonded *A* sites relieve lattice strain by site mixing but can also display structural distortions. For example, $SrBi_2Nb_2O_9$ and $CaBi_2Nb_2O_9$ are orthorhombic while $BaBi_2Nb_2O_9$ has tetragonal symmetry [2].

The effect of systematic substitutions of alkaline earth into the Aurivillius structure have been performed in the two-layer structures [2,5], but not in the three-layer structures. We have therefore undertaken the first systematic study of the effects of the alkaline earth average ionic radius vs. structural stability by replacing Sr^{2+} with varying amounts of Ca^{2+} and Ba^{2+} in $Bi_2Sr_2Nb_2TiO_{12}$. Neutron and X-ray powder diffraction structure refinements were performed as well as bond valence sum calculations to better understand the $n = 3$ Aurivillius ceramics and their potential as fast ion conductors.

2. Experimental procedure

2.1. Powder synthesis and characterization

Powder samples were made using solid state synthesis. A 30 g batch was prepared for each compound. The initial powder reactants Bi_2O_3 99.99% (Alfa), $SrCO_3$ 99.99% (Alfa), $CaCO_3$ 99.99% (Alfa), $BaCO_3$ 99.75% (Alfa), Nb_2O_5 99.99% (Alfa), and TiO_2 99.9% (Alfa) were weighed in stoichiometric proportions. The powders were ground in acetone using a diamonite mortar and pestle until a homogeneous slurry was obtained. The dried slurry was placed in a covered 4×8 cm MgO crucible (Ozark) and heated to 700°C for 5 h at a rate of 150°C/h and cooled. The powder was ground again by hand and fired again to 750°C a second and third time to obtain a homogeneous precursor powder. A portion of the powder was pressed into a pellet using a 1.3 cm diameter steel die under 28 MPa and the pellet was buried in a sacrificial powder bed of the remaining powder in a 30 mL MgO crucible. The crucible was covered and fired to an initial temperature of 1000°C for 12 h, followed by sequential grinding, pressing, and heating in the powder bed to 1100°C three times.

Finally, powder from each sample was pressed into a pellet and sintered at 1050°C for 40 h for impedance measurements and scanning electron microscopy (SEM). SEM samples were mounted in epoxy by vacuum impregnation and polished to a 6 μm finish. Each pellet was electroded using Pt paste for AC impedance measurements. AC impedance spectroscopy experiments were performed using a Solartron 1260 Impedance Gain-Phase Analyzer. Five probe two-point measurements were employed on pellet samples using platinum wire leads. All data files were compensated using open and short circuit measurements according to the method prescribed by Mason et al. [34]. Impedance

measurements were taken over a 10 Hz–10 MHz range from high to low frequency. Data was collected isothermally after a 10 min equilibration at each temperature.

Chemical analysis using inductively coupled plasma atomic emission spectroscopy (ICP) and X-ray fluorescence (XRF) was conducted by a contract laboratory after dissolution in acid and borate fusion, respectively.

2.2. Structure analysis

All X-ray diffraction experiments were performed using a Siemens D500 diffractometer in Bragg–Brentano geometry with a graphite diffracted beam monochromator using fixed 0.3° divergence slits. Measurements for Rietveld refinements were made using a tube power of 40 kV and 30 mA over a range of 2–150°2θ with a 0.02°2θ step size and a 10 s count time. Samples were loaded in top-loaded sample holders and were spun at 50 rpm during the diffraction measurement.

All neutron diffraction experiments were performed using the Special Environment Powder Diffractometer (SEPD) located at the Intense Pulsed Neutron Source (IPNS) at Argonne National Laboratory. Approximately 10 g of each powder was pressed into pellets and stacked in a vanadium sample holder. Room temperature time of flight (TOF) diffraction measurements were collected using four detector banks at 22°, 44°, 90°, and 145°. Combined X-ray and neutron diffraction Rietveld refinements were performed on the data for each of the specimens using GSAS [35] with the EXPGUI [36] implementation.

The initial structural model for the three-layer Aurivillius phase was taken from work by Hervoches and Lightfoot [9] who characterized $Bi_{1.8}Sr_{2.2}Nb_{2.2}Ti_{1.8}O_{12}$ using combined X-ray and neutron diffraction refinements. The X-ray data were refined using the profile function with the Thompson–Cox–Hastings [35] asymmetry correction to handle low-angle peak asymmetry. The neutron data were refined using the modified Von Dreele [37] (GSAS type 3) TOF neutron powder diffraction profile shape.

BVS calculations were performed using bond lengths generated by the refinements with the constants in the BVS formalism taken from the compilation of Brown and Altermatt [38]. Total BVS values for cation sites with mixed occupancy were calculated by simply using the fractional site occupancies.

3. Results and discussion

3.1. Phase stability

Phase purity and bulk chemistry were confirmed using diffraction and ICP/XRF analysis. Visual confirmation of phase purity was also obtained using secondary and backscattered SEM analysis. Fig. 1 shows the X-ray diffraction patterns for the five samples in which all lines can be indexed in the correct space group, $I4/mmm$.

Fig. 2 shows typical secondary (SE) and backscattered electron (BSE) SEM images for pellets sintered to 70% theoretical density. No image contrast was observed in the BSE image, indicating phase purity at the bulk scale.

Table 1 displays the molar chemical composition for each sample obtained from ICP and XRF analyses which are in good agreement with expected values. The slightly low Nb values obtained using XRF are most likely due to incomplete borate fusions [39].

In total, five different samples were synthesized to phase purity. Table 2 shows all of the samples attempted. It was not possible to completely substitute Ca^{2+} or Ba^{2+} for Sr^{2+}. It is interesting to note that the $Bi_2SrCaNb_2TiO_{12}$ and $Bi_2SrBaNb_2TiO_{12}$ compositions represent rough solubility limits.

3.2. Structure refinements

Two initial structure refinements were performed for each composition to clarify two points. Firstly,

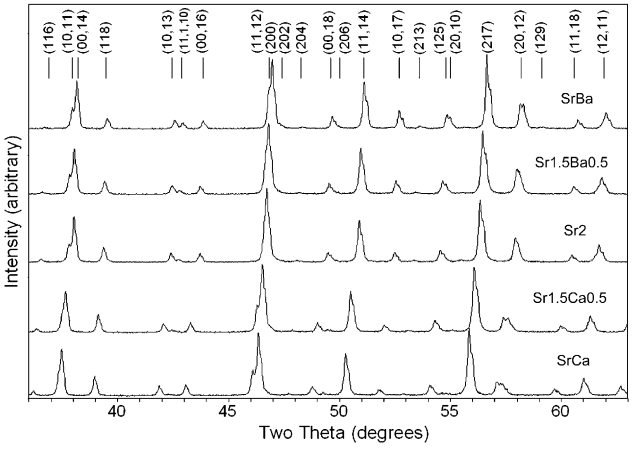

Fig. 1. X-ray diffraction patterns for the pure three-layer Aurivillius compounds with varying alkaline earth chemistry. All lines are indexed as indicated by the stick pattern shown above the data.

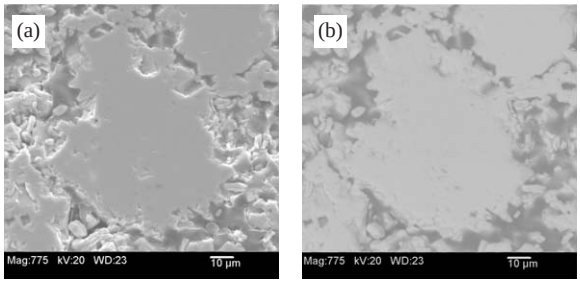

Fig. 2. Secondary (a) and backscattered (b) electron SEM images of a cross-section of a $Bi_2Sr_{1.5}Ba_{0.5}Nb_2TiO_{12}$ pellet.

Table 1
Molar chemical composition for each sample determined using ICP and XRF

Sample	Bi	Sr	Ca	Ba	Nb	Ti
$Bi_2SrCaNb_2TiO_{12}$	2.0	1.0	1.1	0	1.9	1.1
$Bi_2Sr_{1.5}Ca_{0.5}Nb_2TiO_{12}$	1.9	1.5	0.5	0	1.8	1.0
$Bi_2Sr_2Nb_2TiO_{12}$	1.9	1.8	0	0	1.8	1.0
$Bi_2Sr_{1.5}Ba_{0.5}Nb_2TiO_{12}$	1.9	1.5	0	0.5	1.7	1.0
$Bi_2SrBaNb_2TiO_{12}$	1.8	0.9	0	1.1	1.8	1.0

Table 2
Three-layer Aurivillius compositions attempted

Sample	Phase purity
$Bi_2Ca_2Nb_2TiO_{12}$	No
$Bi_2Ca_{1.5}Sr_{0.5}Nb_2TiO_{12}$	No
$Bi_2SrCaNb_2TiO_{12}$	Yes
$Bi_2Sr_{1.5}Ca_{0.5}Nb_2TiO_{12}$	Yes
$Bi_2Sr_2Nb_2TiO_{12}$	Yes
$Bi_2Sr_{1.5}Ba_{0.5}Nb_2TiO_{12}$	Yes
$Bi_2SrBaNb_2TiO_{12}$	Yes
$Bi_2Ba_{1.5}Sr_{0.5}Nb_2TiO_{12}$	No
$Bi_2Ba_2Nb_2TiO_{12}$	No

substitution of the alkaline earths on the Bi site in the $(Bi_2O_2)^{2+}$ layer is expected to result in the alkaline earth adopting a more isotropic position because of the lack of the lone pair of electrons. Initial attempts to refine the data with the alkaline earth constrained to the Bi position resulted in negative thermal parameters.

Secondly, the experimental sensitivity to site mixing was tested by refining the data without constraints on the fractional occupancies of each mixed cation site. The refinements produced accurate values for mixing between the Bi and *A* sites, with the sum of occupancies of the *A* site and Bi site within 5% of unity. Nonetheless, because the final refinements included site mixing between the perovskite *B* sites, all occupancies were constrained to reproduce the known bulk stoichiometry. The fractional occupancies were constrained using the method prescribed by Louer et al. [40].

After completing the initial refinements, full analysis including BVS analysis was undertaken. The full refinements were then divided into two parts, the first following previous work in the field where the oxygen stoichiometry is fixed, resulting in large oxygen thermal parameters on two sites and very large BVS values for the Ti and Nb sites [9,30,31]. The next and final step was to constrain all oxygen thermal parameters to reasonable values and refine oxygen occupancies, which will be discussed in the context of the measured electrical conductivity values.

Fig. 3 shows a typical final result of the combined X-ray and neutron refinement, in this case for the $Bi_2Sr_{1.5}Ba_{0.5}Nb_2TiO_{12}$ composition. A slight mismatch

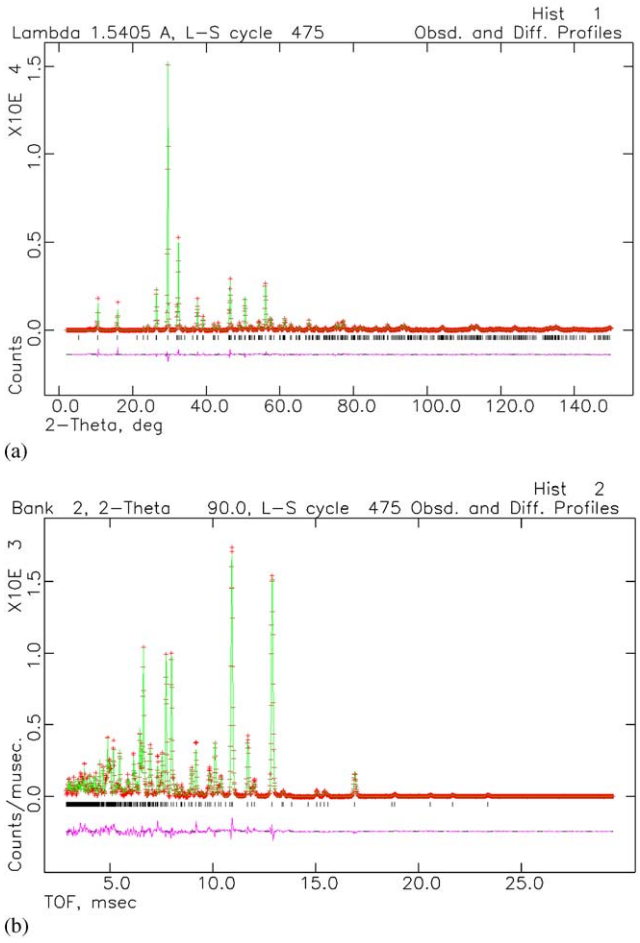

Fig. 3. Final X-ray (a) and neutron (b) Rietveld refinement plots for $Bi_2Sr_{1.5}Ba_{0.5}Nb_2TiO_{12}$.

in the XRD data is observed low angles because of difficulties in modelling peak asymmetry. Tables 3–7 show the refined atomic coordinates, fractional site occupancies and isotropic thermal parameters for the five samples. Table 8 displays all of the refined bond lengths. Fig. 4 shows the linear or nearly linear dependence of the lattice constants on the ACR.

Two major structural features were clearly observed from the refinements. Firstly, the site mixing between the perovskite *A* site and the Bi site was established, as well as mixing among the perovskite *B* sites containing Nb and Ti. Secondly, the relaxation of the alkaline earths when located on the Bi site was observed.

Fig. 5 depicts the static disorder between the Bi and *A* sites. As mentioned previously, the cation mixing between the Bi and *A* sites was constrained to a one-to-one atom exchange. Although there is no well-defined trend in site mixing with ACR, the amount of mixing ranges from 12% to 18%, with larger values at larger ACR.

Fig. 6 displays the total alkaline earth content on the Bi site along with the fraction of Ca^{2+} or Ba^{2+}

Table 3
Refined atomic data for $Bi_2SrCaNb_2TiO_{12}$

*I*4/*mmm*		$a = 3.87106(3)$ Å		$c = 33.0576(4)$ Å		
Atom	Site	Fraction	*x*	*y*	*z*	*U* (100 * Å^2)
Bi^{3+}	Bi	0.46(2)	0	0	0.2134(1)	1.3(1)
Sr^{2+}	Bi	0.08(2)	0	0	0.196(1)	1.3(1)
Bi^{3+}	Bi	0.39(2)	0	0	0.2134(1)	1.3(1)
Ca^{2+}	Bi	0.06(2)	0	0	0.196(1)	1.3(1)
Bi^{3+}	A	0.03(2)	0	0	0.0629(2)	2.1(2)
Sr^{2+}	A	0.41(2)	0	0	0.0629(2)	2.1(2)
Bi^{3+}	A	0.10(2)	0	0	0.0629(2)	2.1(2)
Ca^{2+}	A	0.44(2)	0	0	0.0629(2)	2.1(2)
Nb^{5+}	Nb	0.745(6)	0	0	0.3739(2)	0.4(1)
Ti^{4+}	Nb	0.255(6)	0	0	0.3739(2)	0.4(1)
Ti^{4+}	Ti	0.49(1)	0	0	0.5	0.0(3)
Nb^{5+}	Ti	0.51(1)	0	0	0.5	0.0(3)
O	O1	1	0	0.5	0	7.2(5)
O	O2	1	0	0.5	0.25	1.1(2)
O	O3	1	0	0	0.4421(3)	3.4(4)
O	O4	1	0	0	0.3198(4)	4.3(4)
O	O5	1	0	0.5	0.1159(2)	2.4(2)
$wR_p = 10.1\%$			$\chi^2 = 3.82$			

Table 4
Refined atomic data for $Bi_2Sr_{1.5}Ca_{0.5}Nb_2TiO_{12}$

*I*4/*mmm*		$a = 3.88124(3)$ Å		$c = 33.1266(4)$ Å		
Atom	Site	Fraction	*x*	*y*	*z*	*U* (100 * Å^2)
Bi^{3+}	Bi	0.47(2)	0	0	0.2134(1)	1.7(1)
Sr^{2+}	Bi	0.03(2)	0	0	0.197(2)	1.7(1)
Bi^{3+}	Bi	0.41(2)	0	0	0.2134(1)	1.7(1)
Ca^{2+}	Bi	0.09(2)	0	0	0.197(2)	1.7(1)
Bi^{3+}	A	0.03(2)	0	0	0.06263(1)	2.5(2)
Sr^{2+}	A	0.72(2)	0	0	0.06263(1)	2.5(2)
Bi^{3+}	A	0.09(2)	0	0	0.06263(1)	2.5(2)
Ca^{2+}	A	0.16(2)	0	0	0.06263(1)	2.5(2)
Nb^{5+}	Nb	0.757(6)	0	0	0.3734(1)	0.6(1)
Ti^{4+}	Nb	0.243(6)	0	0	0.3734(1)	0.6(1)
Ti^{4+}	Ti	0.513(9)	0	0	0.5	0.3(4)
Nb^{5+}	Ti	0.486(9)	0	0	0.5	0.3(4)
O	O1	1	0	0.5	0	5.4(4)
O	O2	1	0	0.5	0.25	1.5(2)
O	O3	1	0	0	0.4418(3)	2.9(3)
O	O4	1	0	0	0.3190(3)	3.8(3)
O	O5	1	0	0.5	0.1167(2)	2.3(2)
$wR_p = 8.26\%$			$\chi^2 = 3.24$			

occupying the Bi site. Of the total amount of alkaline earth occupying the Bi site, a substantial fraction comes from Sr^{2+} for the Ca^{2+} compositions, indicating that Ca^{2+} prefers to remain on the *A* site. For the Ba^{2+} compositions, the alkaline earth cations occupying the Bi site appear to be completely Ba^{2+}, while Sr^{2+} remains on the *A* site along with the remaining Ba^{2+}.

As pointed out by Armstrong and Newnham [29] the $(Bi_2O_2)^{2+}$ layer constrains the size of the perovskite block. Site mixing, therefore, occurs to equilibrate the lattice dimensions between the $(Bi_2O_2)^{2+}$ layers and the perovskite block. The refinement results directly support the theory of Armstrong and Newnham [29].

Table 5
Refined atomic data for $Bi_2Sr_2Nb_2TiO_{12}$

*I*4/*mmm*		$a = 3.89257(2)$ Å			$c = 33.1876(3)$ Å	
Atom	Site	Fraction	*x*	*y*	*z*	*U* (100 * Å^2)
Bi^{3+}	Bi	0.864(9)	0	0	0.2142(1)	1.7(1)
Sr^{2+}	Bi	0.1316(9)	0	0	0.197(1)	1.7(1)
Bi^{3+}	A	0.864(9)	0	0	0.06296(1)	2.5(2)
Sr^{2+}	A	0.136(9)	0	0	0.06296(1)	2.5(2)
Nb^{5+}	Nb	0.761(6)	0	0	0.3729(1)	0.6(1)
Ti^{4+}	Nb	0.239(6)	0	0	0.3729(1)	0.6(1)
Ti^{4+}	Ti	0.522(9)	0	0	0.5	0.9(3)
Nb^{5+}	Ti	0.477(9)	0	0	0.5	0.9(3)
O	O1	1	0	0.5	0	4.4(3)
O	O2	1	0	0.5	0.25	2.0(2)
O	O3	1	0	0	0.4414(2)	2.0(2)
O	O4	1	0	0	0.3181(3)	3.6(3)
O	O5	1	0	0.5	0.1179(2)	1.5(2)
$wR_p = 8.65\%$			$\chi^2 = 3.12$			

Table 6
Refined atomic data for $Bi_2Sr_{1.5}Ba_{0.5}Nb_2TiO_{12}$

*I*4/*mmm*		$a = 3.90596(2)$ Å		$c = 33.4777(3)$ Å		
Atom	Site	Fraction	*x*	*y*	*z*	*U* (100 * Å^2)
Bi^{3+}	Bi	0.49(2)	0	0	0.2150(1)	1.4(1)
Sr^{2+}	Bi	0.01(2)	0	0	0.199(1)	1.4(1)
Bi^{3+}	Bi	0.34(2)	0	0	0.2150(1)	1.4(1)
Ba^{2+}	Bi	0.16(2)	0	0	0.199(1)	1.4(1)
Bi^{3+}	A	0.01(2)	0	0	0.0629(1)	2.1(1)
Sr^{2+}	A	0.74(2)	0	0	0.0629(1)	2.1(1)
Bi^{3+}	A	0.16(2)	0	0	0.0629(1)	2.1(1)
Ba^{2+}	A	0.09(2)	0	0	0.06229(1)	2.1(1)
Nb^{5+}	Nb	0.762(6)	0	0	0.3731(1)	0.1(1)
Ti^{4+}	Nb	0.238(6)	0	0	0.3731(1)	0.1(1)
Ti^{4+}	Nb	0.524(9)	0	0	0.5	0.0(3)
Nb^{5+}	Nb	0.476(9)	0	0	0.5	0.0(3)
O	O1	1	0	0.5	0	2.8(3)
O	O2	1	0	0.5	0.25	1.2(2)
O	O3	1	0	0	0.4415(2)	2.0(3)
O	O4	1	0	0	0.3186(2)	2.53(2)
O	O5	1	0	0.5	0.1174(1)	1.0(2)
$wR_p = 8.07\%$			$\chi^2 = 2.65$			

The Bi site is eight coordinated, with a Bi ionic radius of 1.17 Å whereas Ca^{2+} in eightfold coordination is 1.12 Å [41]. Substitution of Ca^{2+} on the Bi site will not reduce the interlayer strain, but substitution of the much larger Ba^{2+}, for example, will reduce the strain.

Site mixing was also observed on the perovskite *B* sites as shown in Fig. 7. The degree of static disorder between the Nb and Ti sites does not change significantly with ACR. Approximately 25% Ti^{4+} occupies the Nb site. An increase in the Ti^{4+} content on the Nb site was observed for the $Bi_2SrCaNb_2TiO_{12}$ composition, but the error bars indicate that the Nb–Ti disorder is probably invariant with ACR.

The driving force for site mixing between the Nb and Ti sites is not clear, but site mixing within the perovskite

Table 7
Refined atomic data for $Bi_2SrBaNb_2TiO_{12}$

I4/mmm		$a = 3.92203(2)$ Å		$c = 33.6642(3)$ Å		
Atom	Site	Fraction	x	y	z	U $(100 * Å^2)$
Bi^{3+}	Bi	0.49(2)	0	0	0.2154(1)	1.8(1)
Sr^{2+}	Bi	0.01(2)	0	0	0.198(1)	1.8(1)
Bi^{3+}	Bi	0.32(2)	0	0	0.2154(1)	1.8(1)
Ba^{2+}	Bi	0.18(2)	0	0	0.198(1)	1.8(1)
Bi^{3+}	A	0.01(2)	0	0	0.0633(1)	2.8(1)
Sr^{2+}	A	0.49(2)	0	0	0.0633(1)	2.8(1)
Bi^{3+}	A	0.18(2)	0	0	0.0633(1)	2.8(1)
Ba^{2+}	A	0.32(2)	0	0	0.0633(1)	2.8(1)
Nb^{5+}	Nb	0.757(6)	0	0	0.3728(1)	0.5(1)
Ti^{4+}	Nb	0.242(6)	0	0	0.3728(1)	0.5(1)
Ti^{4+}	Nb	0.514(9)	0	0	0.5	0.3(3)
Nb^{5+}	Nb	0.485(9)	0	0	0.5	0.3(3)
O	O1	1	0	0.5	0	2.1(2)
O	O2	1	0	0.5	0.25	1.9(2)
O	O3	1	0	0	0.4416(2)	2.3(2)
O	O4	1	0	0	0.3188(2)	2.7(2)
O	O5	1	0	0.5	0.1180(1)	1.5(1)
$wR_p = 7.63\%$			$\chi^2 = 2.44$			

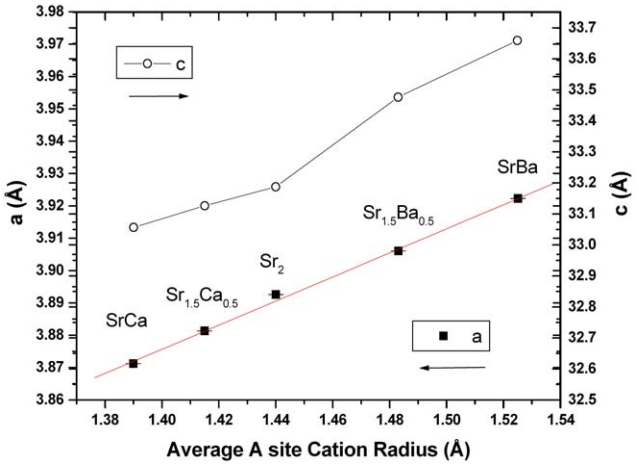

Fig. 4. Refined *a* and *c* lattice parameters versus average alkaline earth cation radius.

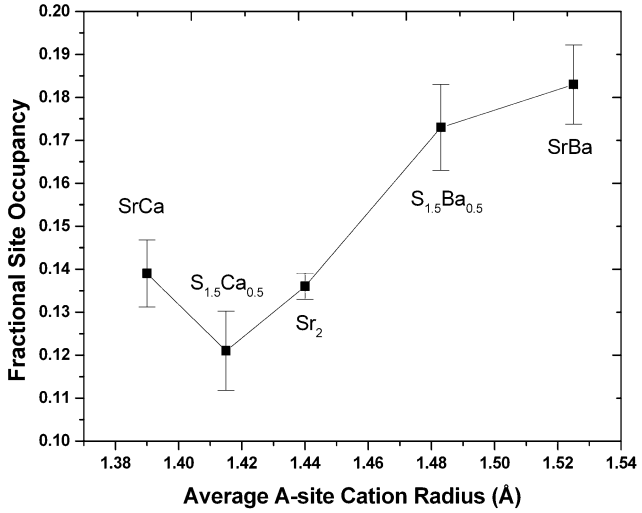

Fig. 5. Fractional occupancy of the *A* cation on the Bi site versus ACR. The fraction of Bi on the *A* is not shown because it was constrained to be equal. Error bars are one estimated standard deviation.

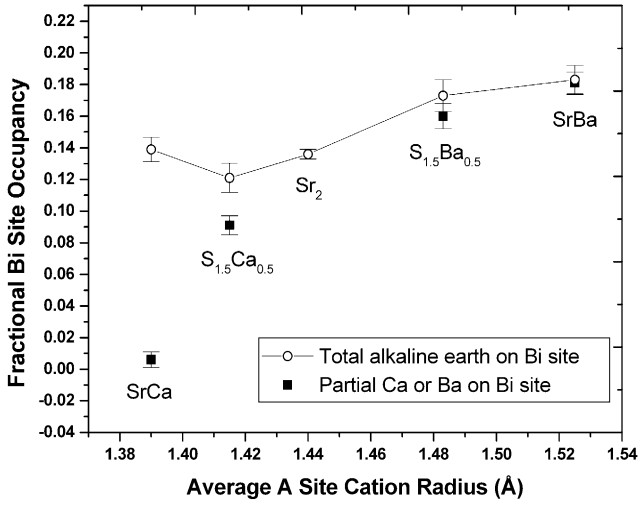

Fig. 6. Fractional occupancy of the Ca or Ba cation occupying the Bi site and total fraction alkaline earth occupying the Bi site versus ACR. Note, the total fraction alkaline earth represents the total quantity of Sr^{2+} and Ca^{2+} or Ba^{2+}. Error bars are one estimated standard deviation.

block will randomize the distribution of two different ions with different radii, resulting in a more homogeneous structural unit.

Finally, the position of the alkaline earth when located on the Bi site changes with cation radius. Tables 3–7 show that the Ca, Sr, and Ba relax to more isotropic *z* coordinates because they lack the lone pair. Because the relaxation of the alkaline earth cation on the host Bi site is small, the BVS was calculated without additional alkaline earth–oxygen bonds. Previous work included alkaline earth–O5 bonds in the BVS calculation [9] but Table 8 shows that the *A* (on Bi site)–O5 bond lengths are at least 3.27 Å for all compositions, which is rather long even for a Ba–O bond, and therefore omitted from the BVS calculation.

Table 9 shows the calculated BVS for the four cation sites in the five compounds. The trends may be observed clearly via Fig. 8. The Bi site BVS remains relatively constant with ACR and is slightly underbonded for all compositions. The expected BVS for the Bi site is on the order of 2.85 for 15% mixing of the alkaline earth with Bi, while the observed values range from 2.55 to 2.75. The *A* site BVS increases with Ba^{2+} substitution and decreases with Ca^{2+} substitution. Because the expected BVS is 2.15 for 15% mixing, the trend ranges from underbonded at the high Ca concentrations to overbonded at the high Ba compositions. It is interesting to note that the *A* site BVS increases with ACR despite the

fact that the *A*–O bond lengths increase with ACR and the fraction of Bi^{3+} occupying the *A* site increases slightly with ACR. These two factors would normally cause a *decrease* in the *A* site BVS, however, Ba^{2+} is large enough to negate any decrease in BVS. The *A* site BVS increase is due solely to the type of alkaline earth occupying the *A* site and is not affected by variations in bond length or site mixing.

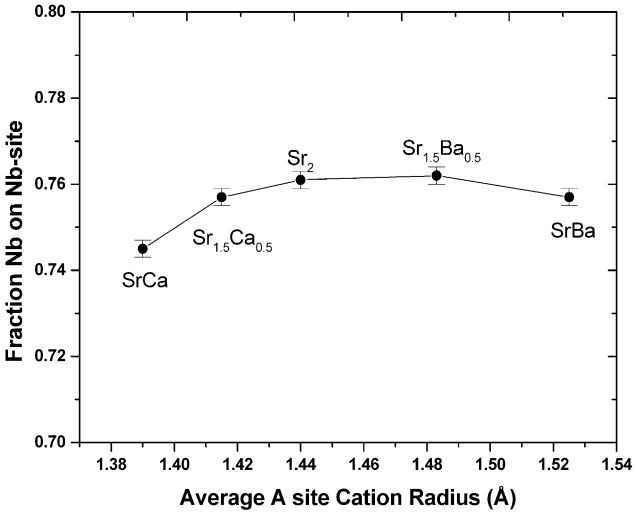

Fig. 7. Fraction Nb^{5+} occupying Nb site versus ACR. Error bars are one estimated standard deviation.

The Nb and Ti site BVS values decrease with increasing ACR because the Nb–O bond lengths increase with ACR. However, the Ti BVS is extremely high for the Ca^{2+} compositions. The expected Ti site BVS for a 50% Nb^{5+} occupancy is 4.5. Therefore, the Ti site BVS values of above 5 are exceedingly high.

Refined thermal parameters shed some light on the unreasonably high Ti BVS. Fig. 9 shows the O1 and O4 thermal parameters plotted as a function of ACR. The O1 anion is in the equatorial plane of the TiO_6 octahedron, and its thermal parameter is extremely large for the Ca^{2+} composition, and decreases to a reasonable value on reaching the $Bi_2SrBaNb_2TiO_{12}$ composition. Furthermore, the O4 thermal parameter is higher than expected, although it is less than one-half of the value for the O1 oxygen. The O4 oxygen site connects the Bi and Nb cations.

The large O1 and O4 oxygen thermal parameter and/or large BVS in the TiO_6 octahedron has been observed in several three-layer Aurivillius phases $Bi_{1.8}Sr_{2.2}Nb_{2.2}Ti_{1.8}O_{12}$ [9], $Bi_4Ti_3O_{12}$ [31], and $Bi_{2.5}Na_{1.5}Nb_3O_{12}$ [30] and in Ruddleson–Popper phases [42]. In the particular study of Hervoches and Lightfoot [31], Rietveld refinements of high temperature neutron powder diffraction measurements indicate that the O1

Table 8
Bond lengths for the five samples

Site	Bond	$Bi_2SrCaNb_2TiO_{12}$	$Bi_2Sr_{1.5}Ca_{0.5}Nb_2TiO_{12}$	$Bi_2Sr_2Nb_2TiO_{12}$	$Bi_2Sr_{1.5}Ba_{0.5}Nb_2TiO_{12}$	$Bi_2SrBaNb_2TiO_{12}$
	Bi–O2	2.2785(6)	2.2837(5)	2.2776(5)	2.2774(5)	2.2815(5)
	Bi–O4	2.9523(17)	2.9524(10)	2.9551(9)	2.9838(8)	3.0030(7)
Bi	*A*–O2	2.581(8)	2.679(24)	2.580(7)	2.589(5)	2.636(4)
	A–O4	2.8026(26)	2.7805(24)	2.8099(20)	2.8265(15)	2.8287(12)
	A–O5	3.338(10)	3.207(11)	3.324(8)	3.361(6)	3.323(5)
	A–O1	2.8357(12)	2.8440(10)	2.8560(10)	2.8728(8)	2.8960(8)
A	*A*–O3	2.74146(17)	2.74842(12)	2.75575(11)	2.76577(10)	2.77824(10)
	A–O5	2.6198(15)	2.6494(12)	2.6640(12)	2.6748(10)	2.6904(9)
	Nb–O3	2.2430(29)	2.2580(23)	2.2641(22)	2.2875(20)	2.3163(18)
Nb	Nb–O4	1.7924(33)	1.7994(28)	1.8189(27)	1.8205(23)	1.8167(21)
	Nb–O5	1.9627(4)	1.96489(32)	1.97092(32)	1.97810(27)	1.98516(24)
Ti	Ti–O1	1.93553(2)	1.94066(1)	1.94628(1)	1.95298(1)	1.96101(1)
	Ti–O3	1.9206(25)	1.9323(19)	1.9557(18)	1.9613(16)	1.9653(14)

Table 9
Bond valence sum values for the five samples

Site	$Bi_2SrCaNb_2TiO_{12}$	$Bi_2Sr_{1.5}Ca_{0.5}Nb_2TiO_{12}$	$Bi_2Sr_2Nb_2TiO_{12}$	$Bi_2Sr_{1.5}Ba_{0.5}Nb_2TiO_{12}$	$Bi_2SrBaNb_2TiO_{12}$
Bi site	2.59	2.56	2.63	2.74	2.68
A site	1.99	2.13	2.15	2.19	2.36
Nb site	4.94	4.86	4.79	4.69	4.63
Ti site	5.10	4.95	4.82	4.68	4.61

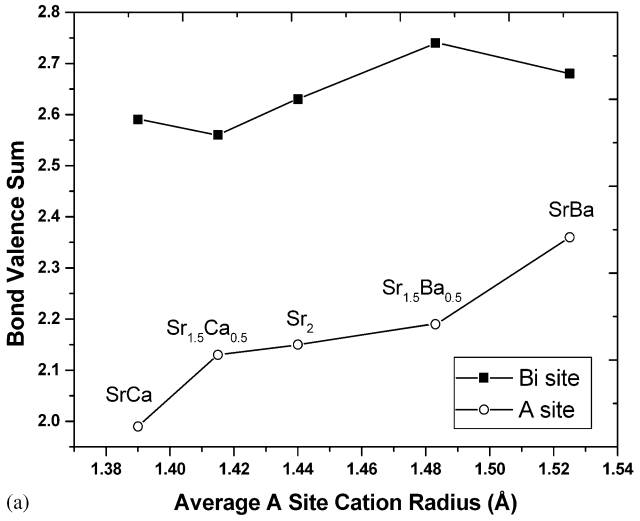

(a)

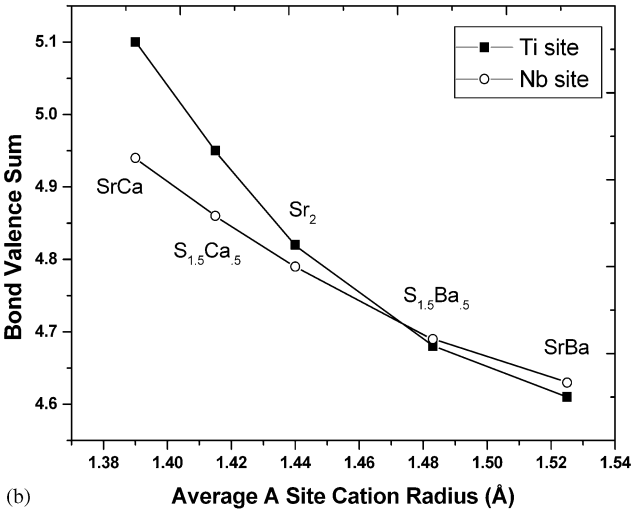

(b)

Fig. 8. Bond valence sum for the Bi and *A* sites (a) and Nb and Ti sites (b) versus ACR.

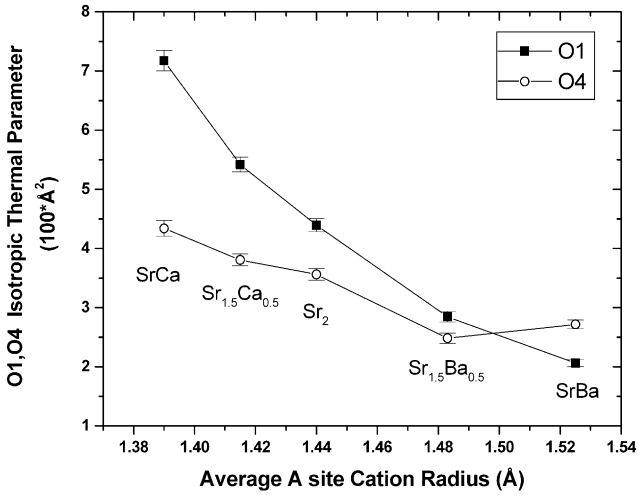

Fig. 9. O1 and O4 oxygen isotropic thermal parameters for all five compositions. Error bars are one estimated standard deviation.

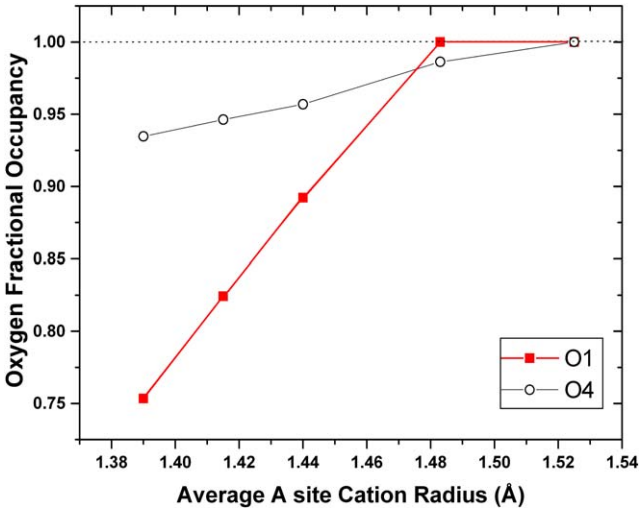

Fig. 10. Refined O1 and O4 oxygen fractional occupancy versus ACR for the five compositions after fixing the thermal parameters.

thermal parameter increases and the Ti site BVS becomes overbonded as the crystal symmetry increases. Borg et al. [30] studied $Bi_{2.5}Na_{1.5}Nb_3O_{12}$ which has an overbonded NbO_6 octahedron (Nb replaces Ti in this structure) as well as large O1 and O4 oxygen thermal parameters. While not presented in their paper, BVS values were calculated for $Bi_{1.8}Sr_{2.2}Nb_{2.2}Ti_{1.8}O_{12}$ using the structure refined by Hervoches and Lightfoot [9] from the bond lengths they provided, the Ti site was found to be highly overbonded with a BVS of 4.99. Wright and Greaves [42] discovered that rotations of the TiO_6 octahedra were necessary to describe the structure of a Ruddleson–Popper phase $Na_2La_2Ti_3O_{10}$ with a layered structure similar to that of an Aurivillius phase.

Additional refinements were therefore attempted in the present work using a model that allowed rotation of the TiO_6 octahedra to determine if indeed the original structure model was correct. Any displacement of the O1 oxygen from its symmetry-fixed position resulted in additional peaks that were clearly visible in the calculated neutron diffraction patterns, thus eliminating the model used in the Ruddleson–Popper phases. In addition, refinements were attempted using the lower symmetry space group *B*2*cb*. However, only the *I*4/*mmm* model proved reasonable.

Finally, the present structures were refined by fixing the O1 and O4 thermal parameters to a reasonable value (0.025 $Å^2$) and refining all of the oxygen occupancies. A clear trend was observed in the O1 and O4 occupancies versus ACR as shown in Fig. 10. The BVS values were of course reduced to more reasonable values across the compositional range, as demonstrated in Fig. 11. In addition, the occupancy of the O4 oxygen, which also had a large thermal parameter, refined to values between

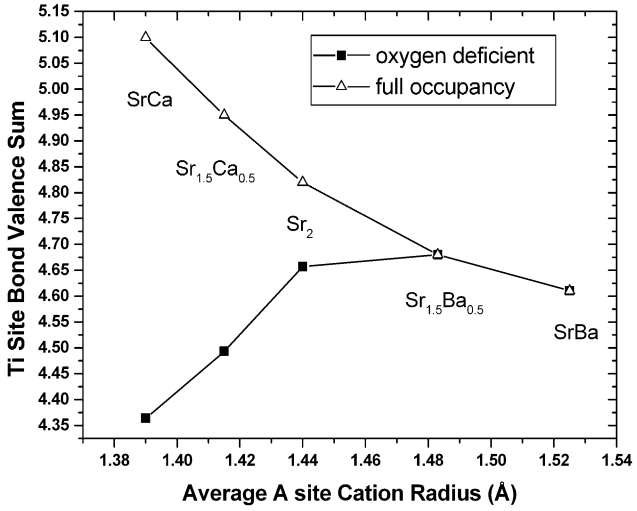

Fig. 11. Ti site BVS recalculated to account for the O1 oxygen deficiency versus ACR for the five compositions.

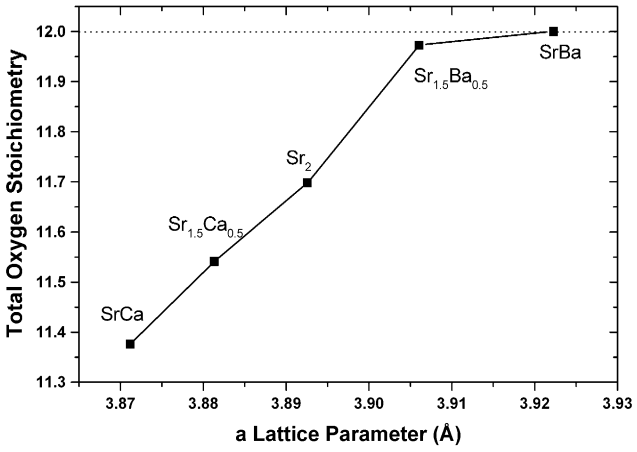

Fig. 12. Total oxygen stoichiometry as a function of a lattice parameter for the five compositions after fixing the thermal parameters.

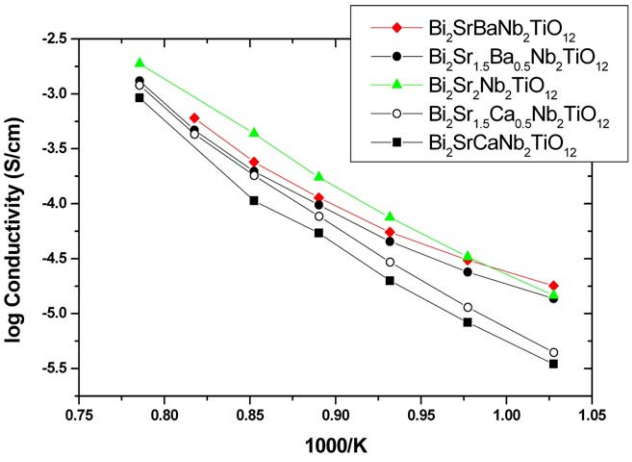

Fig. 13. Arhennius plot of log electrical conductivity versus $1000/T$ of the five compositions obtained from AC impedance spectroscopy.

0.9 and 1, indicating possible oxygen deficiency on that site as well. The degree of oxygen deficiency is significant but not unreasonably large in the context of the unit cell; the total oxygen deficiency ranged from 0.6% to 4.2% vacancies. The total oxygen deficiency possible in pure bismuth oxide is 25% at high temperature in the FCC gamma phase [43,44], while many other Bi-based ionic conductors, notably the Bi$MeVOX$ phases, contain up to 13% oxygen vacancies [43]. Fig. 12 shows the total oxygen stoichiometry as a function of a lattice parameter. The Ca containing compositions would be expected to show some level of oxygen anion conductivity due to the large oxygen deficiency. It should be noted that an oxygen deficiency of any kind must be accompanied by either cation reduction or a cation vacancy. Although none of the cations present are prone to reduction, the Ti or Nb cations are the most likely to take on reduced valence. Unfortunately, no direct evidence of cation reduction or cation vacancies is available.

The electrical conductivity of the specimens was measured using AC impedance and the results are shown in Fig. 13. Note that there are no significant differences in the magnitude of the conductivity nor the activation enthalpy when measured in air. In fact, the Ca containing compositions showed the lowest conductivities of all compositions despite the possible oxygen deficiency. Activation enthalpies for all specimens are on the order of 1.4 eV in the temperature range of 500–1000°C. Although detailed measurements of the electrical behavior have not been performed to determine the type of charge carrier, the mobilities of O^{2-} ions were calculated using the Nernst equation by using the magnitude of the conductivity, 10^{-4} S/cm at 900°C. The number of charge carriers was calculated for each compound using the refined oxygen stoichiometry of each respective composition to obtain carrier concentrations on the order of 10^{22} cm^{-3}. These calculations indicate that the O^{2-} mobilities are extremely low, on the order of 10^{-10} cm^2/V s, compared to typical fast ion conductors which have mobilities on the order of 10^{-4} cm^2/V s [45].

High-temperature neutron diffraction and additional electrical measurements are planned to identify the charge carrier and to determine the oxygen stoichiometry as a function of temperature.

4. Conclusions

Cation site mixing between the Bi and perovskite A sites and between the Nb and Ti sites was observed to occur in three-layer Aurivillius ceramics where Ca^{2+} or

Ba^{2+} was systematically substituted for Sr^{2+} in the base $Bi_2Sr_2Nb_2TiO_{12}$ lattice. The static disorder occurred to reduce interlayer strain between the $(Bi_2O_2)^{2+}$ layer and the perovskite blocks as evidenced by the systematic preference of Ba^{2+} instead of Ca^{2+} for the Bi site.

Three structural complexities were observed, including an unreasonably large thermal parameter for the O1 site in the equatorial plane of the TiO_6 octahedron, a large O4 thermal parameter on the O4 site connecting the Bi and Nb sites, and an unusually large Ti BVS, all of which have been observed previously [9,30,31,42]. Rotation of the TiO_6 octahedra to yield a more accurate structure and reduce the Ti BVS, which has been successful for other layered Bi-based materials [42], did not result in reasonable structure refinements. However, allowing for oxygen deficiency on two sites, the O1 equatorial site in the TiO_6 octahedron and the O4 connecting Bi and Nb, produced a model with reasonable Ti BVS values across the compositional range while incorporating reasonable thermal parameters for the O1 oxygen anion. Both structural models, taken together, demonstrate that there exists significant disorder in the oxygen sublattice within the perovskite blocks. Measurements of the electrical conductivity of each of the five phases supports the oxygen deficient structural model. Additional high-temperature neutron diffraction experiments, pair distribution functions and electrical measurements are planned to better understand the cation disorder in these structures.

Acknowledgments

The authors thank Dr. Jim Jorgensen for use of the SEPD facilities and Simine Short for running the neutron diffraction experiments. The SEPD is supported by the Department of Energy under Contract W-31-109-ENG-38. Primary financial support was provided by the NYS College of Ceramics with partial support by the National Science Foundation Contract DMR9983801.

References

[1] B. Aurivillius, Arkiv fur Kemi 58 (1) (1949) 499–512.
[2] S. Blake, M.J. Falconer, M. McCreedy, P. Lightfoot, J. Mater. Chem. 7 (8) (1997) 1609–1613.
[3] T. Rentschler, Mater. Res. Bull. 32 (3) (1997) 351–369.
[4] N. Yasuda, M. Miyayama, T. Kudo, Solid State Ion. 133 (3–4) (2000) 273–278.
[5] R. Macquart, B.J. Kennedy, Y. Shimakawa, J. Solid State Chem. 160 (1) (2001) 174–177.
[6] R.L. Withers, J.G. Thompson, A.D. Rae, J. Solid State Chem. 94 (2) (1991) 404–417.
[7] K. Kendall, J.K. Thomas, H.-C. zur Loye, Chem. Mater. 7 (1) (1995) 50–57.
[8] W.J. Yu, Y.I. Kim, D.H. Ha, J.H. Lee, Y.K. Park, S. Seong, H.H. Hur, Solid State Commun. 111 (12) (1999) 705–709.
[9] C.H. Hervoches, P. Lightfoot, J. Solid State Chem. 153 (1) (2000) 66–73.
[10] Ismunandar, B.J. Kennedy, J. Mater. Chem. 9 (3–4) (1999) 541–544.
[11] C.H. Hervoches, A. Snedden, R. Riggs, S.H. Kilcoyne, P. Manuel, P. Lightfoot, J. Solid State Chem. 164 (2) (2002) 280–291.
[12] E.C. Subbarao, Phys. Rev. 122 (3) (1961) 804–807.
[13] P. Duran-Martin, A. Castro, P. Millan, B. Jimenez, J. Mater. Res. 13 (9) (1998) 2565–2570.
[14] H.S. Shulman, M. Testorf, D. Damjanovic, N. Setter, J. Am. Ceram. Soc. 79 (12) (1996) 3124–3128.
[15] J.K. Thomas, K. Kendall, H.-C. zur Loye, Solid State Ion. 70/71 (1) (1994) 225–228.
[16] M.S. Peterson, Synthesis optimization of Aurivillius Phases, M.S. Thesis, NYS College of Ceramics at Alfred University, Alfred, New York, 2003.
[17] S.A. Speakman, The crystal chemistry of brownmillerite- and N = 3 Aurivillius-type ceramic conductors for fuel cell applications, Ph.D. Thesis, NYS College of Ceramics at Alfred University, Alfred, New York, 2003.
[18] C. Say, Electrical and compositional study of $n = 3$ Aurivillius structures for oxygen conducting devices, M.S. Thesis, NYS College of Ceramics at Alfred University, Alfred, New York, 2002.
[19] S. Borg, G. Svensson, J. Solid State Chem. 157 (1) (2001) 160–165.
[20] P. Boullay, G. Trolliard, D.Mercurio, J.M. Perez-Mato, L. Elcoro, J. Solid State Chem. 164 (2) (2002) 252–260.
[21] P. Boullay, G. Trolliard, D.Mercurio, J.M. Perez-Mato, L. Elcoro, J. Solid State Chem. 164 (2) (2002) 261–271.
[22] L. Minervini, R.W. Grimes, K.E. Sickafus, J. Am. Ceram. Soc. 83 (8) (2000) 1873–1878.
[23] K.W. Eberman, B.J. Wuensch, J.D. Jorgensen, Solid State Ion. 148 (3–4) (2002) 521–526.
[24] J.-E. Jorgensen, A.J. Markvardsen, Physica C 349 (1–2) (2001) 25–29.
[25] M.A.L. Field, C.S. Knee, M.T. Weller, J. Solid State Chem. 167 (1) (2002) 237–244.
[26] A.D. Robertson, H. Tukamoto, J.T.S. Irvine, J. Electrochem. Soc. 146 (11) (1999) 3958–3962.
[27] V.M. Goldschmidt, E.B.A. Muir, Geochemistry, Oxford University Press, London, 1962.
[28] D.Y. Suárez, I.M. Reaney, W.E. Lee, J. Mater. Res. 16 (11) (2001) 3139–3149.
[29] R.A. Armstrong, R.E. Newnham, Mater. Res. Bull. 7 (10) (1972) 1025–1034.
[30] S. Borg, G. Svensson, J.-O. Bovin, J. Solid State Chem. 167 (1) (2002) 86–96.
[31] C.H. Hervoches, P. Lightfoot, Chem. Mater. 11 (11) (1999) 3359–3364.
[32] A.D. Rae, J.G. Thompson, R.L. Withers, A.C. Willis, Acta Crystallogr. B 46 (4) (1990) 474–487.
[33] C.O. Paiva-Santos, Powder Diffr. 15 (2) (2000) 134–138.
[34] D.D. Edwards, J.-H. Hwang, S.J. Ford, T.O. Mason, Solid State Ion. 99 (1–2) (1997) 85–97.
[35] A.C. Larson, R.B.V. Dreele, General structure analysis system (GSAS), Los Alamos National Laboratory Report LAUR 86-748, 1994.
[36] B.H. Toby, J. Appl. Crystallogr. 34 (2001) 210–213.
[37] R.B. Von Dreele, J.D. Jorgensen, C.G. Windsor, J. Appl. Crystallogr. 15 (2) (1982) 581–589.
[38] I.D. Brown, D. Altermatt, Acta Crystallogr. B 41 (4) (1985) 244–247.
[39] N. Mozola, Lakefield Research Inc. Ontario, March 2003, private communication.
[40] J.-M. Louer, R. Cerny, M. Latroche, A. Percheron-Guegan, K. Yvon, J. Appl. Crystallogr. 31 (3) (1998) 327–332.

[41] R.D. Shannon, Acta Crystallogr. A 32 (1) (1976) 751–767.
[42] A.J. Wright, C. Greaves, J. Mater. Chem. 6 (11) (1996) 1823–1825.
[43] N.M. Sammes, G.A. Tompsett, H. Näfe, F. Aldinger, J. Eur. Ceram. Soc. 19 (10) (1999) 1801–1826.
[44] S. Boyapati, E.D. Wachsman, B.C. Chakoumakos, Solid State Ion. 138 (3–4) (2001) 293–304.
[45] T. Ishihara, J.A. Kilner, M. Honda, N. Sakai, H. Yokokawa, Y. Takita, Solid State Ion. 113–115 (12) (1998) 593–600.